Journal of Materials Chemistry A

ROYAL SOCIETY OF CHEMISTRY

PAPER

View Article Online
View Journal

Cite this: DOI: 10.1039/d5ta08830e

Ultrathin defective Fe_2O_{3-x} skins on exsolved nanoparticles from a perovskite cathode enable highly active and sulfur-tolerant CO_2 electroreduction

Sehun Choi,†[a] Jungseub Ha,†[a] Sanghwa Jeong,[b] Hansol Bae,[a] Jeongbin Cho,[a] Sujin Kim,[a] Yongju Yun[a] and Won Bae Kim*[ab]

Solid oxide electrolysis cells (SOECs) have emerged as a promising application for electrochemically converting CO_2 to CO, presenting a feasible strategy to mitigate industrial CO_2 emissions. Among various gas streams, blast furnace gas (BFG), a byproduct from steel making, contains high concentrations of CO_2 and impurities such as H_2S, which severely impact CO_2 conversion efficiency and cathode durability due to sulfur poisoning. Herein, a double perovskite system of $Sr_{1.6}Pr_{0.4}Fe_{1.35}Ni_{0.2}Mo_{0.45}O_{6-\delta}$ (SPFNM), functionalized with *in situ* exsolved $FeNi_3$ alloy nanoparticles (NPs) encapsulated by ultrathin Fe_2O_{3-x} layers *via* steam-assisted wet reduction (wet-SPFNM) was developed as a novel cathode for SOECs. This tailored $FeNi_3/Fe_2O_{3-x}$ core–shell nanostructure provides additional oxygen vacancies for CO_2 electrolysis active sites and enhances sulfur tolerance, attributed to a defect-rich Fe_2O_{3-x} shell that effectively protects the metallic core by oxidizing adsorbed H_2S. A single cell with a wet-SPFNM cathode showed a current density of 568 mA cm^{-2} at 1.3 V and 750 °C, approximately 38% higher than the conventional dry-reduced SPFNM (dry-SPFNM), containing exsolved metallic $FeNi_3$ alloy NPs. Furthermore, the wet-SPFNM cathode demonstrated excellent operational stability, showing negligible degradation over 100 h at 750 °C at a constant current of 250 mA cm^{-2} under BFG conditions. This research highlights the potential of exsolved core–shell NPs as a robust design strategy for sulfur-tolerant SOEC cathodes operating in realistic industrial gas environments.

Received 30th October 2025
Accepted 10th February 2026

DOI: 10.1039/d5ta08830e

rsc.li/materials-a

Introduction

The continuous increase in atmospheric carbon dioxide (CO_2) concentration, primarily driven by the combustion of fossil fuels and intensive industrial activities, poses one of the most pressing environmental challenges of our time. As a primary greenhouse gas, CO_2 substantially contributes to global warming, necessitating urgent development of effective mitigation technologies.[1] Among various industrial sources, blast furnace gas (BFG), a byproduct of steel manufacturing primarily composed of N_2, CO_2, CO, and H_2 with trace amounts of H_2S, benzene (C_6H_6), CH_4, and H_2O, contributes approximately 7–9% of global CO_2 emissions.[2,3] Thus, the capture and utilization of CO_2 in BFG may serve as a crucial approach to mitigating the carbon emissions associated with industrial operations.[4] Given its large volume and continuous emission from industrial processes, BFG represents a major target for carbon capture and utilization (CCU) technologies. Through electrochemical reduction of CO_2 and recovery of CO as a valuable fuel, BFG can be effectively converted into useful products, offering significant environmental and economic benefits in the treatment of industrial waste gases. The practical implementation of CCU technologies under the continuously emitted stream of BFG requires both high CO_2 conversion efficiency and long-term catalyst durability, especially under harsh industrial gas conditions that include various impurities such as H_2S and C_6H_6.[5] Among the diverse CCU approaches, solid oxide electrolysis cells (SOECs) have emerged as promising electrochemical systems for efficient CO_2 conversion and renewable energy storage, owing to their inherent advantages including low overpotentials, high current densities, and exceptional faradaic and energy efficiencies under elevated-temperature operating conditions.[6,7] These characteristics position SOECs as a carbon-neutral platform for production of chemical fuels and value-added products from CO_2, thereby facilitating the realization of sustainable energy cycles.

Conventionally, Ni-based cermet electrodes, particularly Ni-YSZ (yttria-stabilized zirconia), have been employed as SOEC

[a]Department of Chemical Engineering, Pohang University of Science and Technology (POSTECH), 77 Cheongam-ro, Nam-gu, Pohang-si, Gyeongsangbuk-do 37673, Republic of Korea. E-mail: kimwb@postech.ac.kr

[b]Department of Battery Engineering, Graduate Institute of Ferrous & Eco Materials Technology (GIFT), Pohang University of Science and Technology (POSTECH), 77 Cheongam-ro, Nam-gu, Pohang-si, Gyeongbuk-do 37673, Republic of Korea

† These authors contributed equally to this work.

cathodes due to their superior electrocatalytic activity toward CO_2 reduction.[8] However, their practical implementation is hindered by carbon deposition (coking),[9] susceptibility to oxidation under high oxygen partial pressure (pO_2) atmospheres[10] and sulfur poisoning.[11,12] To address these limitations, perovskite oxides (ABO_3) are promising alternative electrode materials: single, double and Ruddlesden–Popper (R–P) layered structures provide mixed ionic–electronic conductivity (MIEC), redox stability, and intrinsic resistance to carbon deposition.[13–16] In particular, $Sr_2Fe_{1.5}Mo_{0.5}O_{6-\delta}$ double perovskite oxide offers high electronic conductivity and stability in both oxidizing and reducing atmospheres.[17] Despite these benefits, their catalytic activity remains inferior to that of Ni-based cermet cathodes, primarily due to insufficient chemical adsorption and activation of nonpolar CO_2 molecules at elevated temperatures.[6] To boost the catalytic performance of perovskites, *in situ* exsolution of metallic nanoparticles (NPs) from the lattice has been extensively investigated.[18–20] This approach not only generates catalytically active metal-oxide interfaces but also induces the formation of oxygen vacancies, both of which synergistically facilitate improved CO_2 adsorption, dissociation, and subsequent reduction kinetics.[21] However, similar to Ni-based cermet, these exsolved metallic NPs remain susceptible to sulfur poisoning, which critically restricts their application under realistic industrial gas conditions such as BFG.[22,23] In parallel, metal oxides have been widely utilized as regenerable sorbents for hot-gas desulfurization (HGD), offering a practical means of removing H_2S from high-temperature gas streams.[24–26] Oxides such as Fe_2O_3, ZnO, and CuO demonstrate strong chemical affinity toward H_2S and exhibit redox cyclability without significant degradation. Among them, iron-based oxides are particularly notable for their high sulfur uptake capacity and facile regeneration. This proven capability of iron oxides in HGD processes provides a compelling rationale for integrating their desulfurizing function at the nanoscale to protect SOEC cathodes from sulfur poisoning. Recent studies have reported exsolved metal/oxide core–shell NPs for CO_2 electrolysis; however, in most cases core–shell formation is described mainly as an outcome of a specific reduction protocol, without clearly identifying the governing parameters that determine whether exsolution yields metallic *versus* core–shell nanostructures. In addition, mechanistic evidence and quantitative analyses that directly compare the two exsolved states particularly in terms of surface defect analyses, remain limited, and the potential advantages of core–shell architecture under H_2S-containing (impurity-relevant) conditions remain scarce.[27–29]

Motivated by this, we developed a $Sr_{1.6}Pr_{0.4}Fe_{1.35}Ni_{0.2}Mo_{0.45}O_{6-\delta}$ (SPFNM) double perovskite as a cathode material for CO_2 electrolysis in SOECs under simulated-BFG conditions (CO_2-separated BFG). Here, CO_2-separated BFG denotes a CO_2-rich, BFG derived gas mixture after upstream CO_2 capture and primary desulfurization, and the detailed composition and selection basis are described in the Experimental section of the SI. Steam-assisted exsolution in humidified H_2 (5% H_2O) triggers the *in situ* formation of $FeNi_3$/Fe_2O_{3-x} core–shell NPs (wet-SPFNM) that remain firmly anchored to the perovskite surface. For comparison, a conventional dry reduction under pure H_2 was used to exsolve metallic Fe–Ni alloy NPs (dry-SPFNM), serving as a control to elucidate the role of the core–shell nanostructure in enhancing electrocatalytic activity and sulfur tolerance. The oxygen vacancy-enriched Fe_2O_{3-x} shell provides a high density of active sites for CO_2 electrolysis while mitigating H_2S poisoning by shielding the alloy core and promoting oxidation of adsorbed sulfur species. To elucidate the physico-chemical structure differences between the two types of exsolved nanostructures, various characterization techniques were employed, including X-ray diffraction (XRD) for phase identification, scanning electron microscopy (SEM) and transmission electron microscopy (TEM) for morphological observation, X-ray absorption fine structure (XAFS) for local electronic structures, soft X-ray absorption spectroscopy (XAS) and X-ray photoelectron spectroscopy (XPS) for surface chemical state analysis. Notably, a single cell with the wet-SPFNM cathode achieved 568 mA cm^{-2} at 1.3 V and 750 °C, which is 38% higher than the dry reduced counterpart, and it maintained stable performance with negligible degradation over 100 h under CO_2-separated BFG.

Results and discussion

Structure and microscopic analysis

The crystal structures of pristine, wet- and dry-reduced SPFNM powders were characterized by using X-ray diffraction (XRD). As shown in Fig. 1a, the pristine SPFNM exhibits a well-defined double perovskite structure, consistent with $Sr_{2.0}Fe_{1.5}Mo_{0.5}O_{6-\delta}$ (SFM), with no detectable secondary phases. Notably, compared to SFM, the diffraction peaks of SPFNM exhibited an overall peak shift toward higher 2θ angles, indicative of lattice shrinkage induced by A-site Pr and B-site Ni co-doping, as the ionic radii of Pr^{3+} and Ni^{2+} are much smaller than those of Sr^{2+} and Fe^{3+}, respectively.[30] Upon wet- and dry-reduction at 850 °C for 2 h, all diffraction peaks shifted toward lower 2θ angles, suggesting lattice expansion associated with additional oxygen vacancy formation and decrease in B-site cation oxidation states within the perovskite lattice. Notably, the phase transition was clearly observed, with the emergence of Ruddlesden–Popper (R–P) phase ($Sr_3FeMoO_{7-\delta}$, PDF#01-075-3655) at 31.3°, and $FeNi_3$ (PDF#38-0419) at 44.1°. This result demonstrated that SPFNM partially transforms into the R–P structure, accompanied by the exsolution of B-site transition metal species as described by eqn (1):

$$\begin{aligned} &Sr_{1.6}Pr_{0.4}Fe_{1.35}Ni_{0.2}Mo_{0.45}O_{6-\delta} \\ &\quad + H_2 \rightarrow (Sr,\ Pr)_3Fe_{1-x-y}Ni_xMo_yO_{7-\delta} \\ &\quad + Sr_{1.6}Pr_{0.4}(Fe_{1.35}Ni_{0.2}Mo_{0.45})_{1-z}O_{6-\delta}^{\cdot\cdot} + FeNi_3 + H_2O + V_O^{\cdot\cdot} \end{aligned} \quad (1)$$

To evaluate the redox stability and structural reversibility of SPFNM, *in situ* synchrotron X-ray powder diffraction analysis was performed by holding the wet-SPFNM at 800 °C in an air atmosphere for 10 h (Fig. 1b and S1). During the reoxidation process, the main diffraction peak gradually shifted toward

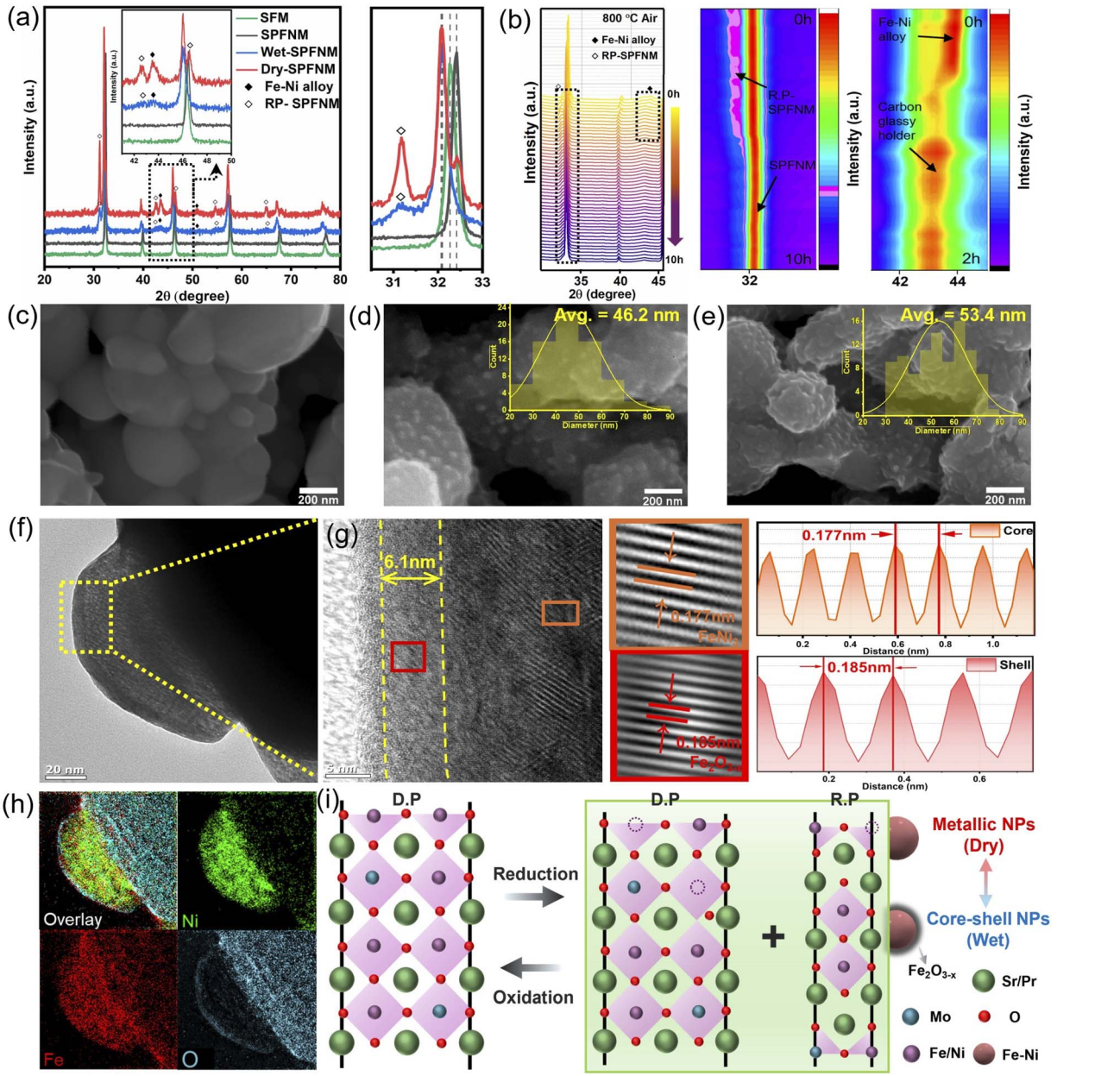

Fig. 1 (a) X-ray diffraction patterns (XRD) of SFM, pristine SPFNM, wet-SPFNM, dry-SPFNM and (b) *in situ* XRD patterns of wet-SPFNM in the range of 30–45° acquired at 800 °C during the 10 h reoxidation process. SEM images of (c) pristine SPFNM, (d) wet-SPFNM and (e) dry-SPFNM. High-resolution TEM (HRTEM) images of exsolved core–shell nanoparticles from wet-SPFNM are shown in (f) and (g), and (h) EELS mapping at the Ni K-edge, Fe K-edge and O K-edge, respectively. (i) Schematics of the phase reversibility of SPFNM during the redox process.

higher 2θ values, indicating oxygen reincorporation into the lattice and the reconstruction of the original double perovskite. This was accompanied by the incremental disappearance of the R–P phase peak at 31.2° over 10 h. In addition, the peak near 44.1°, corresponding to the $FeNi_3$ phase, completely disappeared after approximately 36 min of reoxidation process. These observations suggest that the exsolved NPs were dissolved back into the perovskite lattice, and that the partially transformed R–P structure underwent a phase transformation back to the original double perovskite. To corroborate the structural reversibility suggested by the *in situ* XRD measurements, we conducted *ex situ* SEM analysis on the wet-SPFNM with reoxidation treatment in air for different durations (15 min, 1 h, and 2 h) at 800 °C. The SEM images (Fig. S2) show a progressive decrease in the density of the exsolved NPs with increasing reoxidation time. These morphological changes are fully consistent with the disappearance of the $FeNi_3$ diffraction feature during reoxidation, supporting the gradual redissolution of exsolved nanoparticles back into the perovskite lattice. In addition to its redox reversibility, SPFNM exhibits good material compatibility with the ionic conductor $Ce_{0.9}Gd_{0.1}O_2$ (GDC), as shown in Fig. S3. No secondary phases

were detected, after co-sintering at 1000 °C for 2 h in ambient air, indicating excellent phase stability. The microstructural changes resulting from the reduction process were investigated by SEM and TEM analyses of SPFNM samples before and after reduction. Fig. 1c shows the SEM images of the pristine SPFNM, revealing a smooth surface morphology with an average particle size of approximately 350 nm. Scanning TEM (STEM) with energy dispersive spectroscopy (EDS) analysis further confirmed the homogeneous distribution of elements (Sr, Pr, Fe, Ni, Mo, O) within the pristine particles (Fig. S4). After reduction under both wet- and dry-conditions, numerous NPs were uniformly distributed on the SPFNM matrix, resulting in a roughened morphology, as shown in Fig. 1d and e.

Notably, the exsolved NPs formed under wet conditions exhibited a smaller average particle size (46.2 nm) compared to those formed under dry conditions (53.4 nm). This observation implies that the elevated pO_2 induced by the presence of water vapor (5% H_2O) modulates the reduction environment, thereby influencing the migration and surface diffusion of B-site transition metal cations.[31] Consequently, this leads to the formation of smaller and more uniformly distributed NPs under wet reduction conditions, while dry reduction appears to promote further growth of exsolved NPs on the surface. This finding highlights the importance of reduction conditions in controlling the size and distribution of exsolved NPs. To more quantitatively estimate the accessible active-site density, we additionally analyzed exsolved NPs on bar-pellet samples, which enabled reliable particle counting. The calculated areal coverage values are comparable for wet- and dry-SPFNM (θ = 0.209 and 0.223, respectively), while wet-SPFNM shows a higher interfacial line density (L = 22.4 *vs.* 18.3), and the detailed statistics and calculation procedure are provided in Fig. S5.

Fig. 1f and g present high-resolution TEM (HR-TEM) images of a nanoparticle formed under humidified H_2 (5% H_2O) conditions. The exsolved nanoparticle exhibits socketed morphology with the perovskite oxide support, indicating strong interfacial adhesion between NPs and the substrate. High magnification image shows three distinct regions: an amorphous oxide layer, a shell and a core region. The amorphous layer is attributed to surface oxidation caused by exposure to ambient air at room temperature following the reduction process.[32] The shell region exhibits lattice fringes with 0.185 nm, indexed to the (113) planes of Fe_2O_{3-x} (PDF#47-1409). In contrast, the crystal plane spacing of the core region is 0.177 nm, assigned to the (200) plane of $FeNi_3$ (PDF#38-0419). Furthermore, EELS mapping confirmed that the exsolved nanoparticle primarily consisted of Ni and Fe, whereas the shell region contains a relatively higher oxygen content compared to the core region (Fig. 1h). These observations demonstrate that exsolution under wet-reduction conditions should promote the formation of metal/oxide core–shell NPs, as a result of partial surface oxidation driven by the presence of water vapor.[33] In contrast, HR-TEM images of NPs exsolved under pure H_2 conditions (Fig. S6) revealed the formation of metallic Fe–Ni alloy NPs without any distinct shell region, in line with previous reports on conventional exsolution behavior.[34,35] The absence of a shell layer suggests that the much lower pO_2 in the dry-reduction environment suppresses partial surface oxidation, leading to the direct formation of bare metallic particles on the perovskite surfaces. These observations imply that the pO_2 during the reduction process not only affects exsolution kinetics but also governs the structural evolution, offering a tunable parameter for tailoring nanoarchitecture. To further elucidate the effect of pO_2 on the exsolved particle structure, additional reduction experiments were conducted under a harsh humidified H_2 atmosphere containing ~12% H_2O (designated as 12% wet-SPFNM; Fig. S7). HR-TEM images and EELS mapping reveal that the exsolved NPs under these conditions exhibit a smaller particle size (25.4 nm) and a more pronounced core–shell structure compared to those formed under lower humidity (wet-SPFNM). As shown in Fig. S7b and e, the core and shell regions exhibit *d*-spacings of 0.207 nm and 0.235 nm, corresponding to the (111) plane of Fe–Ni alloy (PDF#47-1405) and the (112) plane of Fe_2O_3 (PDF#47-1409), respectively. Notably, the shell-to-core thickness ratio increased significantly from 0.168 in the wet-SPFNM to 0.491 in the 12% wet-SPFNM, highlighting that the core–shell thickness ratio can be modulated by controlling the pO_2 during the exsolution process. This observation is consistent with previous reports, where elevated pO_2 conditions appeared to promote the formation of thicker oxide shells around exsolved NPs.[36] This reversible structural evolution of SPFNM with exsolved NPs is schematically illustrated in Fig. 1i.

Electronic structure and local coordination evolution of B-site cations

To investigate the oxidation states and relative reducibility of B-site transition metal ions in the perovskite structure, synchrotron-based X-ray absorption spectroscopy (XAS) analysis was performed. The normalized Ni and Fe K-edge XANES spectra of pristine SPFNM and wet-SPFNM samples are shown in Fig. 2a and b, along with reference spectra of Ni and Fe oxides and metallic foil. Upon reduction, the absorption edges of both Ni and Fe in wet-SPFNM shift to lower energies, and a concurrent decrease in white-line resonance intensity are observed. These findings suggest that both the Ni–O and Fe–O bonding interactions are weakened, accompanied by a reduction in the oxidation states of Ni and Fe in the wet-SPFNM.[32,37] Notably, the Ni K-edge absorption edge energy in wet-SPFNM was determined to be 8346.20 eV, representing a significant downshift of 0.78 eV compared to the pristine SPFNM. In contrast, the Fe K-edge exhibited a more modest decrease in binding energy from 7127.58 to 7127.30 eV following wet-reduction, corresponding to a slight shift of 0.28 eV (Fig. S8). The substantially larger binding energy shift for Ni (0.78 eV) compared to Fe (0.28 eV) indicated that Ni exhibits greater susceptibility to reduction compared to Fe, thereby promoting more facile exsolution of Ni at the surface. This trend is consistent with the EELS analysis, which revealed a more prominent Ni signal than Fe in the exsolved nanoparticle. The Fourier-transformed EXAFS spectra at the Ni K-edge, presented in Fig. 2c, exhibit a distinct coordination peak at 1.47 Å, corresponding to the Ni–O scattering path. In the wet-SPFNM sample, the intensity of this Ni–O peak is notably decreased, and a new peak emerges at around 2.20 Å,

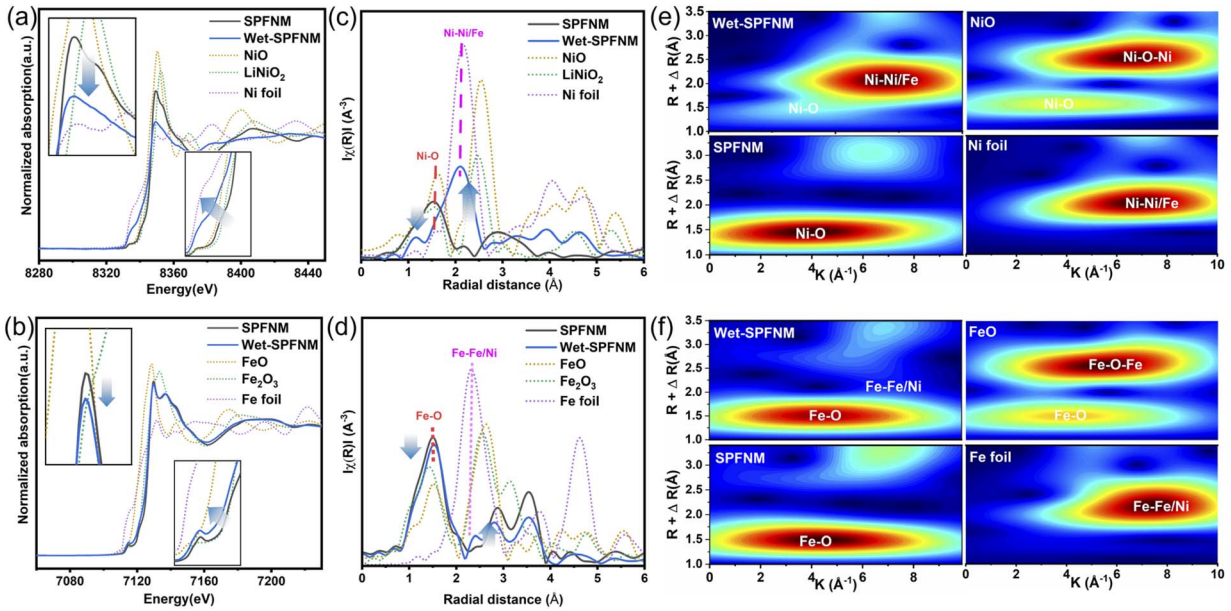

Fig. 2 Synchrotron X-ray absorption fine structure (XAFS). Normalized XANES spectra of pristine SPFNM, wet-SPFNM, and reference samples at the (a) Ni K-edge and (b) Fe K-edge; Fourier-transformed EXAFS spectra at the (c) Ni K-edge and (d) Fe K-edge; and wavelet transform (WT) of the k^2-weighted EXAFS spectra at the (e) Ni K-edge and (f) Fe K-edge for pristine SPFNM, wet-SPFNM and reference samples.

which can be attributed to Ni–Ni or Ni–Fe coordination. Similarly, the Fe K-edge EXAFS spectra in Fig. 2d display a prominent Fe–O coordination peak near 1.46 Å. After wet-reduction, a slight decrease in the Fe–O peak intensity is observed, accompanied by the appearance of a new coordination shell at 2.10 Å, corresponding to Fe–Fe and Fe–Ni bonding. These local structure evolutions suggest the formation of a Fe–Ni alloy phase upon wet-reduction, in agreement with the XANES results.[38] To quantitatively support the coordination changes inferred from the EXAFS, we additionally performed EXAFS fitting for both Ni and Fe K-edges.

The representative fits and key coordination parameters are provided in Fig. S9 and Table S1, showing the reduced B–O coordination and the emergence of a metal–metal contribution after wet-reduction. To further elucidate the local coordination environment, wavelet transform (WT) analysis was performed for both Ni and Fe K-edge EXAFS spectra, enabling simultaneous resolution in both *k*- and *R*-spaces. As shown in Fig. 2e, the k^2-weighted WT contour map of the Ni K-edge in the pristine SPFNM displays a maximum intensity centered around 4 $Å^{-1}$, which is characteristic of Ni–O coordination. In contrast, the wet-SPFNM exhibits a distinct shift of the maximum intensity toward 7 $Å^{-1}$, indicating the presence of Ni–Ni coordination. Similarly, Fig. 2f presents the WT plots of the Fe K-edge. The pristine SPFNM shows a dominant intensity around 3.8 $Å^{-1}$, associated with Fe–O coordination. However, in the wet-SPFNM, a faint WT feature appears at $k \approx 8$ $Å^{-1}$ in the higher-R region, indicating the emergence of Fe–Fe coordination. These results provide further evidence that, under wet-reducing conditions, Ni and Fe are partially reduced and segregated from the perovskite lattice, exsolving to the surface as an Fe–Ni alloy phase.[39]

Surface electronic structure and CO_2 adsorption properties

Soft X-ray absorption spectroscopy (XAS) at the Ni and Fe L-edges was performed to investigate their electronic configurations and valence states, with a focus on the near-surface region. Measurements were conducted in total electron yield (TEY) mode, which is highly surface-sensitive, with a probing depth of approximately 11 nm. The normalized Ni and Fe L-edge XAS spectra of SPFNM, wet-SPFNM, and dry-SPFNM are shown in Fig. 3a and b, respectively, while the corresponding reference spectra are shown in Fig. S10. As shown in Fig. 3a, due to the spin–orbit interaction in the Ni 2p core level, the Ni L-edge spectra display two distinct regions: the L_3-edge (~852 eV, features α and β) and the L_2-edge (~870 eV, features γ and δ).[40] The α and γ peaks are associated with transitions to the 3d t_{2g} states, whereas β and δ are related to the 3d e_g state.[41] The pristine SPFNM exhibits spectral features closely resembling those of NiO (Fig. S10a), indicating a similar surface coordination environment and confirming that Ni exists predominantly in the +2 oxidation state before reduction. In contrast, both wet- and dry-reduced SPFNM samples exhibit markedly different spectral features. The characteristic doublet splitting at the L_2-edge disappears, and the white-line peak α shifts slightly toward lower photon energies. These changes closely resemble the spectral profile of metallic Ni indicating that Ni is predominantly reduced to the Ni^0 state after the reduction.[42,43] As shown in Fig. 3b and S10b, the Fe L-edge spectra also comprise two distinct regions: the L_3-edge around 710 eV (features B, C) and L_2-edge around 723 eV (features D, E). Peaks B and D correspond to the Fe 3d t_{2g} orbit, while peaks C and E are attributed to the Fe 3d e_g orbit. The intensity ratio of e_g/t_{2g} provides qualitative indication of the hole distribution, thereby reflecting the oxidation state of Fe.[44,45] Upon oxidation, electrons are

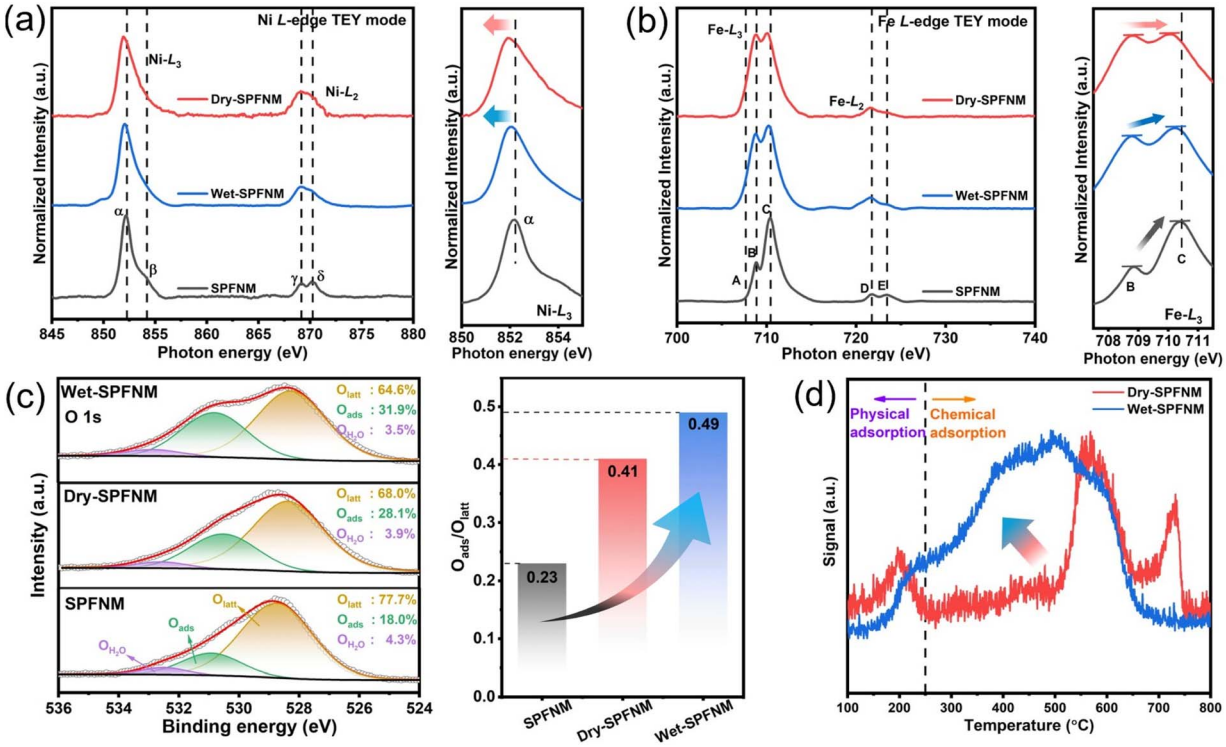

Fig. 3 Normalized soft X-ray absorption spectroscopy (XAS) in TEY mode of (a) Ni L-edge spectra and (b) Fe L-edge spectra of pristine SPFNM, wet-SPFNM, dry-SPFNM. (c) O 1s XPS spectra of pristine SPFNM, wet-SPFNM, dry-SPFNM. (d) CO_2-TPD profile of wet-SPFNM and dry-SPFNM.

preferentially depleted from the e_g orbitals, resulting in enhanced intensity at peak C. The Fe L-edge spectrum of the pristine SPFNM closely resembles that of Fe_2O_3, with an e_g/t_{2g} intensity ratio of 2.12, consistent with 2.08 for Fe_2O_3, thereby confirming the predominance of Fe^{3+} in surface (Table S2).

After reduction, the Fe L-edge spectra of both wet- and dry-SPFNM exhibit noticeable change. A new shoulder peak A appears at a lower photon energy (~707.5 eV) in both reduced samples, which is characteristic of metallic Fe,[46] suggesting partial reduction to Fe^0. More importantly, the e_g/t_{2g} ratio slightly increases to 1.02 for dry-SPFNM and 1.11 for wet-SPFNM, indicating an increase in unoccupied e_g/t_{2g} states, consistent with the presence of more residual oxidized Fe species, which can be attributed to the oxide shell in wet-SPFNM. To further support XAS results, Ni 2p and Fe 3p XPS analyses were conducted (Fig. S11). Metallic Ni and Fe are clearly identified at binding energies of 853.3 and 52.7 eV, respectively.[47,48] Notably, the proportion of oxidized Fe species ($Fe^{3+} + Fe^{2+}$) in wet-SPFNM reached 82.2%, which is higher than 78.4% of dry-SPFNM, indicating structural differences in exsolved particles, in agreement with the XAS results. These results are likely attributed to the formation of an iron oxide shell surrounding the exsolved NPs under wet-reduction conditions. This interpretation is further supported by HR-TEM and EELS analyses, which clearly reveal the presence of a core–shell structure. Furthermore, to gain insight into the oxygen species present on the surface, the O 1s XPS spectra were analyzed. As shown in Fig. 3c, the spectra were deconvoluted into three main peaks located at approximately 528.5 eV, 531.0 eV and 532.8 eV corresponding to lattice oxygen (O_{latt}), adsorbed oxygen species (O_{ads}) and surface hydroxyl/water species (O_{H_2O}) respectively.[49,50] The O_{ads} species are highly sensitive to surface oxygen vacancy sites, which directly reflect the extent of the oxygen vacancies at the surface. In the pristine SPFNM, the ratio of O_{ads}/O_{latt} was only 0.23. However, upon dry-reduction, this ratio increased to 0.41, consistent with the formation of oxygen vacancies resulting from the exsolution of B-site transition metals, as described in eqn (1). Notably, the wet-SPFNM exhibited further increase in the O_{ads}/O_{latt} ratio to 0.49 which can be attributed to the formation of an oxygen defect-rich oxide shell layer in the core–shell NPs, exsolved under wet-reduction conditions. To further investigate the CO_2 adsorption behavior, CO_2 temperature-programmed desorption measurements were conducted and compared for wet-SPFNM and dry-SPFNM, as shown in Fig. 3d. A low-temperature desorption peak below 250 °C, corresponding to physically adsorbed CO_2 species *via* van der Waals forces between the cathode surface and CO_2 molecules,[51,52] appeared similarly in both samples. However, above 250 °C, the wet-SPFNM displayed significantly higher CO_2 desorption capacities compared to the dry-SPFNM. This enhanced CO_2 desorption capacity is attributed to the abundant oxygen vacancies within the oxide shell, which facilitates the formation of bidentate carbonate species upon CO_2 adsorption. In contrast, the dry-SPFNM showed an additional desorption peak around 750 °C, which is likely associated with strongly bound carbonate intermediates stabilized at the interface between the exsolved metallic NPs and the

perovskite substrate, where localized electron-rich regions can facilitate robust CO_2 binding.

Electrochemical characterization

Given that the $FeNi_3/Fe_2O_{3-x}$ core–shell nanostructure in wet-SPFNM features an oxygen defect-rich oxide shell, which can serve as active sites for CO_2 adsorption, electrochemical impedance spectroscopy (EIS) was performed to evaluate the effect on the electrochemical behavior of the cathode materials. The LSGM ($La_{0.8}Sr_{0.2}Ga_{0.8}O_{3-\delta}$) electrolyte-supported single cells with the configuration of SPFNM-GDC|LSGM|LSCF-GDC were fabricated (Fig. S12), and cathodes were fed with CO_2-separated BFG at a total gas flow rate of 50 mL min^{-1} (Fig. S13). Nyquist plots for pristine SPFNM, wet-SPFNM and dry-SPFNM cathode single cells at different applied voltages compared to open circuit voltage (OCV) are presented in Fig. 4a–c. In these plots, the offset between the high- and low-frequency intercepts on the real axis represents the polarization resistance (R_p), a critical parameter for evaluating the electrochemical activity of the electrodes. When the cell voltage was increased from 0.1 to 0.4 V (*vs.* OCV) at 750 °C, the R_p values of the wet-SPFNM cell substantially dropped from 0.947 to 0.474 Ω cm^2. In comparison, the pristine SPFNM and dry-SPFNM cells exhibited more moderate decreases, with R_p values declining from 1.425 to 0.761 Ω cm^2 and from 1.116 to 0.523 Ω cm^2, respectively (Table S3). Notably, the wet-SPFNM cell consistently demonstrated lower resistance compared to the pristine SPFNM and dry-SPFNM single cells under the same operating conditions, demonstrating superior catalytic performance for CO_2 electrolysis. To better understand the electrode reaction mechanisms, distribution of relaxation time (DRT) analysis was performed on the EIS results, accompanied by contour plots to highlight the variation of impedance values with applied voltages. Fig. 4d–f reveal three distinct relaxation processes: P1 (-10^4 Hz) associated with O^{2-} ion transfer at the electrode/electrolyte interface; P2 (10^2–10^3 Hz) involved a charge transfer reaction within the electrode; P3 (10^{-1}–10^1 Hz) corresponds to CO_2 adsorption/desorption kinetics on the cathode surface.[53–55] As shown in Fig. 4g–i, the values of P1 and P2 processes were comparable across the three different cathode cells when the cell voltage was raised from 0.1 to 0.4 V (*vs.* OCV), which can be attributed to the presence of the same LSGM electrolyte and LSCF anode in all configurations. Despite the similar trends observed in P1 and P2 regions, the wet-SPFNM cell exhibited a notable decrease in intensity in the P3 region compared to the counterparts, highlighting its enhanced capability for CO_2 adsorption/desorption.

This observation is consistent with the O 1s XPS and CO_2-TPD results, which indicate that the exsolved core–shell NPs in

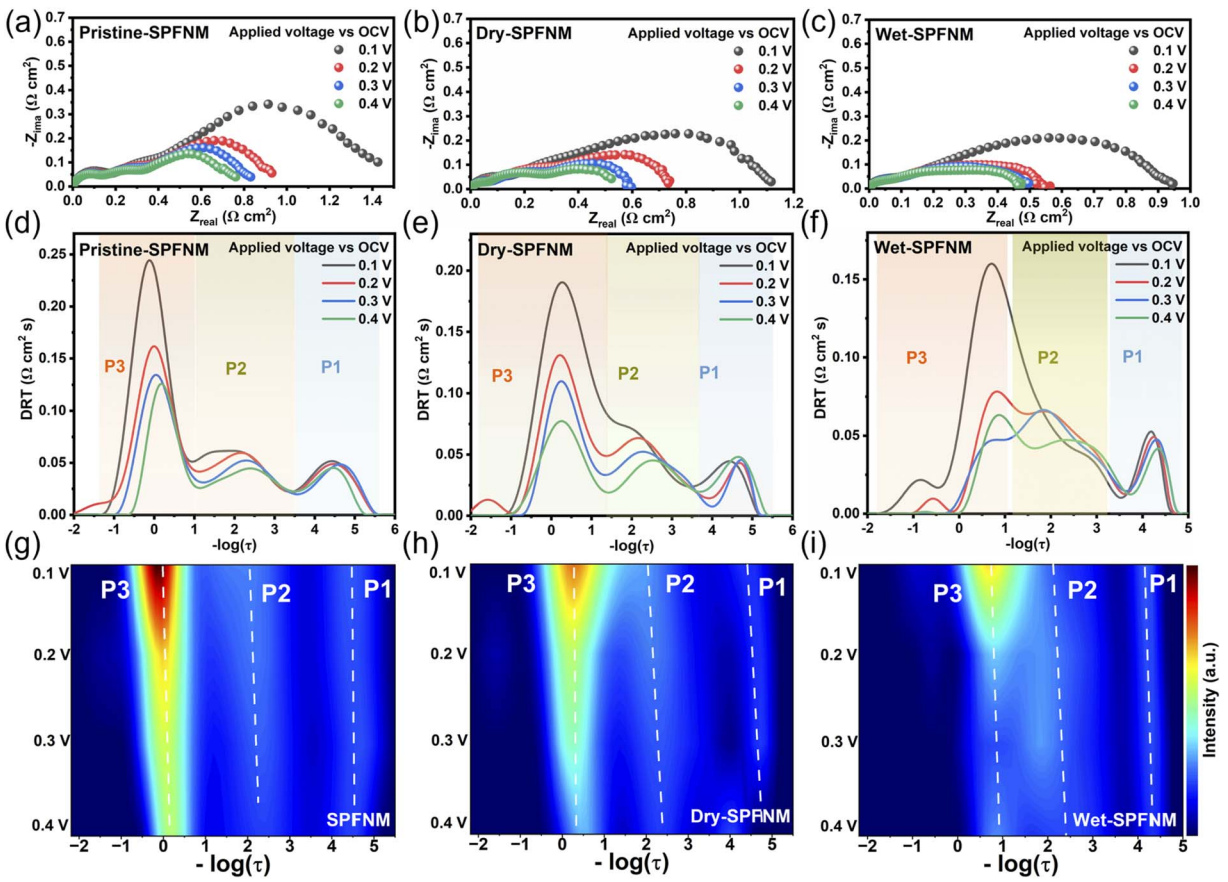

Fig. 4 (a–c) Electrochemical impedance spectroscopy (EIS), (d–f) distribution of relaxation times (DRT), and (g–i) corresponding DRT contour plots of singe cells with pristine, dry- and wet-SPFNM cathodes under various applied potentials (0.1–0.4 V *vs.* OCV) in a CO_2-separated BFG atmosphere at 750°C.

wet-SPFNM provide additional active sites for CO_2 adsorption, thereby enhancing CO_2 electrolysis performance. The *I–V* curves for CO_2 electrolysis with wet-SPFNM and dry-SPFNM cathode single cells are presented in Fig. 5a and S14a. Under an applied voltage of 1.3 V, the cell with the wet-SPFNM cathode achieved current densities of 1.569, 0.990, 0.568, 0.169 A cm^{-2} at 850, 800, 750 and 700 °C, respectively. In contrast, the single cell with the dry-SPFNM cathode exhibited markedly lower performance, reaching current densities of 1.341, 0.854, 0.409 and 0.139 A cm^{-2} under the same conditions. A direct comparison of the current densities at 1.3 V over the range of 850–700 °C for both single cells is summarized in Fig. 5b. With identical electrolyte and anode configurations, the superior CO_2-electrolysis performance of the wet-SPFNM cathode is attributable primarily to its enhanced catalytic activity arising from its distinct exsolved nanostructure, which furnishes abundant active sites for CO_2 adsorption, dissociation, and electrolysis. Notably, the single cell with the wet-SPFNM cathode maintained high CO_2 electrolysis performance even under the more practically relevant CO_2-separated BFG feed containing CO/CO_2 mixtures with additional impurities, showing performance that compares well with literature reports obtained under CO/CO_2-mixture and pure CO_2 conditions (Fig. 5d and Table S6).[56–69] Temperature-dependent EIS further supports these trends (Fig. S14b and c). The high-frequency intersection with the *Z*-axis indicated ohmic resistance (R_s), mainly from the LSGM electrolyte, while the low-frequency intersection shows total cell resistance (R_t). R_p is calculated as the difference between R_t and R_s. As expected from the identical LSGM electrolyte, no significant difference in R_s was observed between the two cells (Tables S4 and S5). While both R_s and R_p values decreased with increasing temperature, the R_p of the wet-SPFNM cell was consistently and significantly lower than that of the dry-SPFNM cell, corroborating its superior catalytic activity observed in the *I–V* curves.

This behavior suggests that the Fe_2O_{3-x} shell does not act as a charge transport-limiting layer under operating conditions, and the performance improvement mainly originates from the

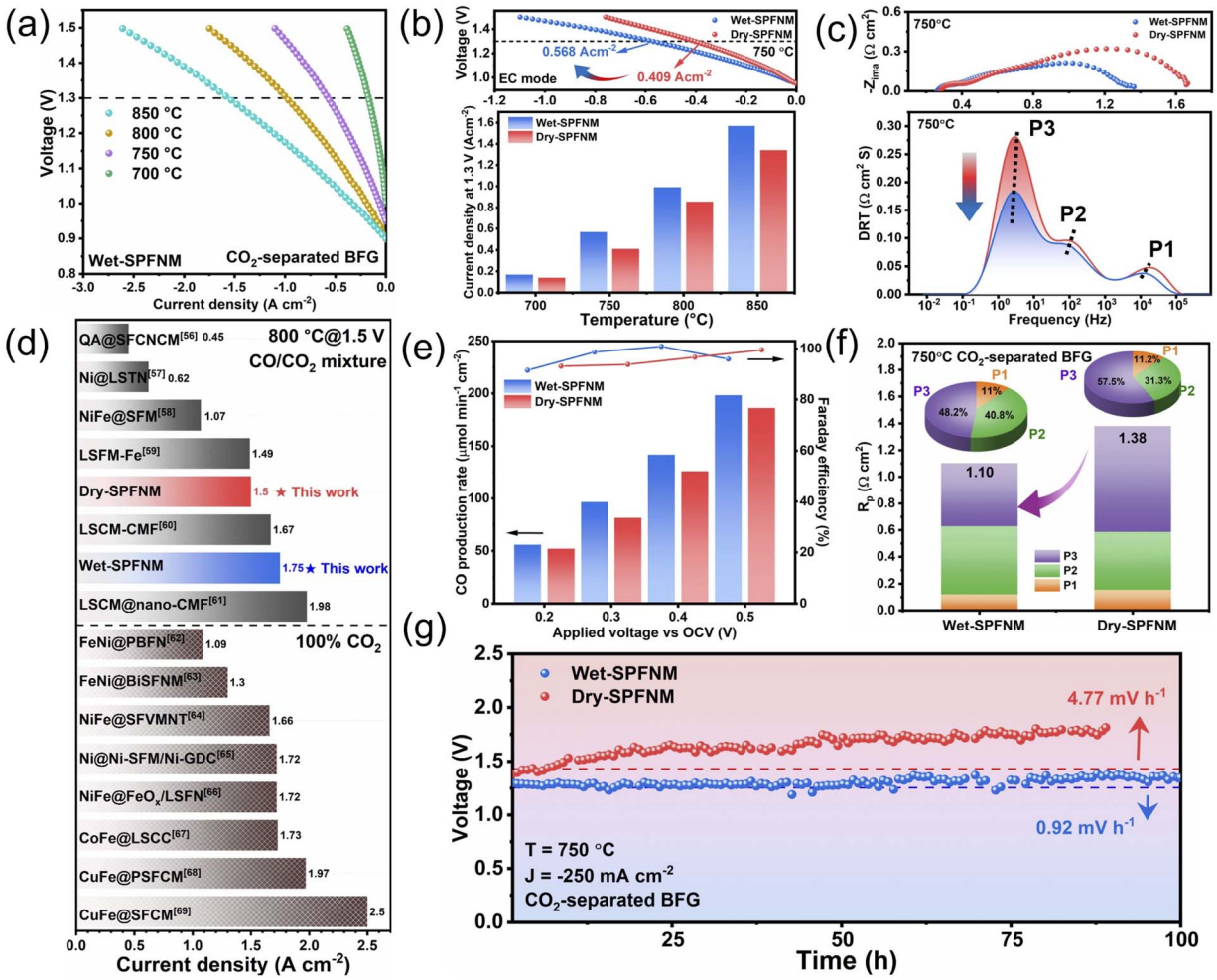

Fig. 5 (a) *I–V* curves, (b) current density at 1.3 V at 850–700 °C and (c) DRT analysis at 750 °C of wet-SPFNM and dry-SPFNM. (d) Performance comparison of cathodes in this study with those from previously reported CO_2 electrolysis studies conducted under CO/CO_2 mixed-gas and 100% CO_2 conditions at 1.5 V.[56–69] (e) The rate of CO production and the corresponding Faraday efficiency under applied voltage. (f) R_p values and its components' contribution (P1, P2, P3) at 750 °C and (g) long-term stability test at the constant current density of 250 mA cm^{-2} at 750 °C under the CO_2-separated BFG conditions.

reduced polarization losses. To deconvolve the specific electrode kinetics, DRT analysis was performed and the DRT peak areas quantified to evaluate the contribution of each electrochemical process (Fig. 5c, S15 and S16). The P3 contribution to R_p, which reflects CO_2 adsorption and desorption and is the largest component, indicates that P3 is the rate determining step (RDS); at 750 °C it constitutes 57.5% of total R_p in the dry SPFNM cell but dramatically decreases to 48.2% in the wet SPFNM cell (Fig. 5f). Furthermore, the apparent activation energies (E_a) for the CO_2RR, derived from the linear Arrhenius plots of R_p, were found to be nearly identical for both wet-SPFNM and dry-SPFNM (Fig. S17). This result suggests a common RDS and thus a similar reaction pathway for both cathodes, therefore, the performance increase in wet-SPFNM arises mainly from decreased surface-process resistance, enabled by the abundance of active sites on its unique nanostructure. The CO production rate and faradaic efficiency of the two single cells under varying applied voltage (*vs.* OCV) are shown in Fig. 5e. The single cell with the wet-SPFNM cathode achieved CO production rates of 55.79, 96.48, 141.72 and 198.23 μmol min^{-1} cm^{-2} at applied voltages of 0.2 to 0.5 V, respectively. In contrast, the dry-SPFNM cathode cell exhibited much lower production rates of 51.94, 81.48, 126.0, and 185.9 μmol min^{-1} cm^{-2} under identical conditions. Meanwhile, the faradaic efficiency remained above 90% for both cells across the entire voltage range. This enhancement can be attributed to the abundant formation of metal/oxide interfaces on the surface, resulting from the *in situ* exsolution of $FeNi_3/Fe_2O_{3-x}$ core–shell nanostructures. These interfaces provide a high density of active sites for CO_2 adsorption, arising from the synergistic interaction between the metallic core and the surrounding oxygen defect-rich oxide shell. The presence of oxygen vacancies within the shell offers CO_2 molecule adsorption sites, while the intimate contact at the metal/oxide interface facilitates efficient electron transfer. Consequently, CO_2 adsorption and activation are favored at these interfacial regions, leading to significant improvement in electrochemical conversion efficiency. Fig. 5g displays the long-term stability test results of single cells with wet-SPFNM and dry-SPFNM cathodes for CO_2 electrolysis at 750 °C under a CO_2-separated BFG atmosphere, operated at a constant current density of 250 mA cm^{-2}. The single cell with the wet-SPFNM cathode maintained stable CO_2 electrolysis for 100 h with a degradation rate of 0.92 mV h^{-1}; in contrast, the dry-SPFNM cell degraded rapidly at 4.77 mV h^{-1}. This fast performance degradation in the dry-SPFNM cathode cell may be attributed to progressive sulfur poisoning of the exsolved Fe–Ni alloy NPs, which deactivates electrocatalytic sites, disrupts interfacial electron-transfer pathways, and causes a loss of CO_2 adsorption sites, thereby resulting in unstable and deteriorating cell performance under CO_2-separated BFG conditions.

Degradation analysis of SOEC cathode materials under BFG conditions

To further investigate the physicochemical changes occurring in both cathode materials under CO_2-separated BFG conditions, wet- and dry-SPFNM powders were treated at 750 °C for 10 h in that atmosphere. Fig. 6a shows the XRD patterns of wet-SPFNM and dry-SPFNM after treatment. Both samples maintained characteristic diffraction peaks of the SPFNM double perovskite structure and the exsolved Fe–Ni alloy at approximately 44°, demonstrating the structural stability of wet-SPFNM, dry-SPFNM and exsolved NPs under these conditions. However, distinct secondary phases were observed. Both samples exhibited a diffraction peak at 27.6°, assigned to $SrMoO_4$ (PDF#08-0482), a phase commonly resulting from the decomposition of Sr-containing perovskites under various fuel environments (*e.g.* CH_4, CO_2, H_2, air).[38,70–73] More notably, an additional secondary phase peak at approximately 25°, corresponding to $SrCO_3$ (PDF#05-0418), exclusively appeared in dry-SPFNM. $SrCO_3$ typically formed through carbonation reactions involving A-site-rich perovskites exposed to a CO_2-containing atmosphere.[74] The emergence of this peak suggests that the dry-SPFNM contained a higher fraction of R–P-SPFNM phases, which are particularly susceptible to decomposition in CO_2-rich environments. To further validate the correlation between the content of R–P phases and $SrCO_3$ formation, a comparative analysis was conducted using R-SFM, dry-SPFNM, and wet-SPFNM (Fig. S18). Upon reduction, pristine SFM was fully transformed into the R–P phase, exhibiting a significantly higher proportion compared to dry-SPFNM and wet-SPFNM. After subsequent treatment under CO_2 at 800 °C for 10 h, the intensity of the $SrCO_3$ diffraction peak followed the same trend: R-SFM > dry-SPFNM > wet-SPFNM, demonstrating that the extent of R–P phase formation directly impacts the degree of surface carbonation in CO_2-rich environments (Fig. S19). As shown in Fig. 6b, c and S20, SEM-EDS analysis confirmed that the exsolved NPs in wet-SPFNM remained well-dispersed and morphologically consistent before and after BFG treatment. In contrast, dry-SPFNM exhibited a non-uniform distribution of NPs, along with noticeable exsolved particle agglomeration and the formation of surface species such as $SrCO_3$, indicating severe surface segregation and structural instability under the same conditions. Furthermore, EDS elemental mapping of carbon revealed localized C signals specifically at the agglomerated regions in dry-SPFNM, further confirming the formation of carbonate species. This interpretation is further supported by the C 1s XPS spectra (Fig. S21), showing an additional carbonate-related peak at 289.5 eV exclusively in dry-SPFNM. However, the absence of D-band (~1340 cm^{-1}) and G-band (~1560 cm^{-1}) signals in the Raman spectra indicates negligible carbon deposition on both samples, suggesting their excellent resistance to carbon coking (Fig. 6d). To assess the impact of hydrocarbon impurities of BFG, wet-SPFNM and dry-SPFNM were treated at 800 °C for 10 h in N_2 containing C_6H_6 (500 ppm) and CH_4 (1 mol%); XRD showed that both samples retain their parent structure, with only a minor $SrMoO_4$ impurity reflection (Fig. S22). These results imply that trace amounts of hydrocarbon impurities in CO_2-separated BFG (*e.g.*, C_6H_6, CH_4) have minimal direct impact on the surface of cathodes. The S 2p XPS spectra of wet-SPFNM and dry-SPFNM are shown in Fig. 6e.

In the dry-SPFNM, two distinct peaks are observed at 161.5 and 162.8 eV, corresponding to S $2p_{3/2}$ and S $2p_{1/2}$, respectively,

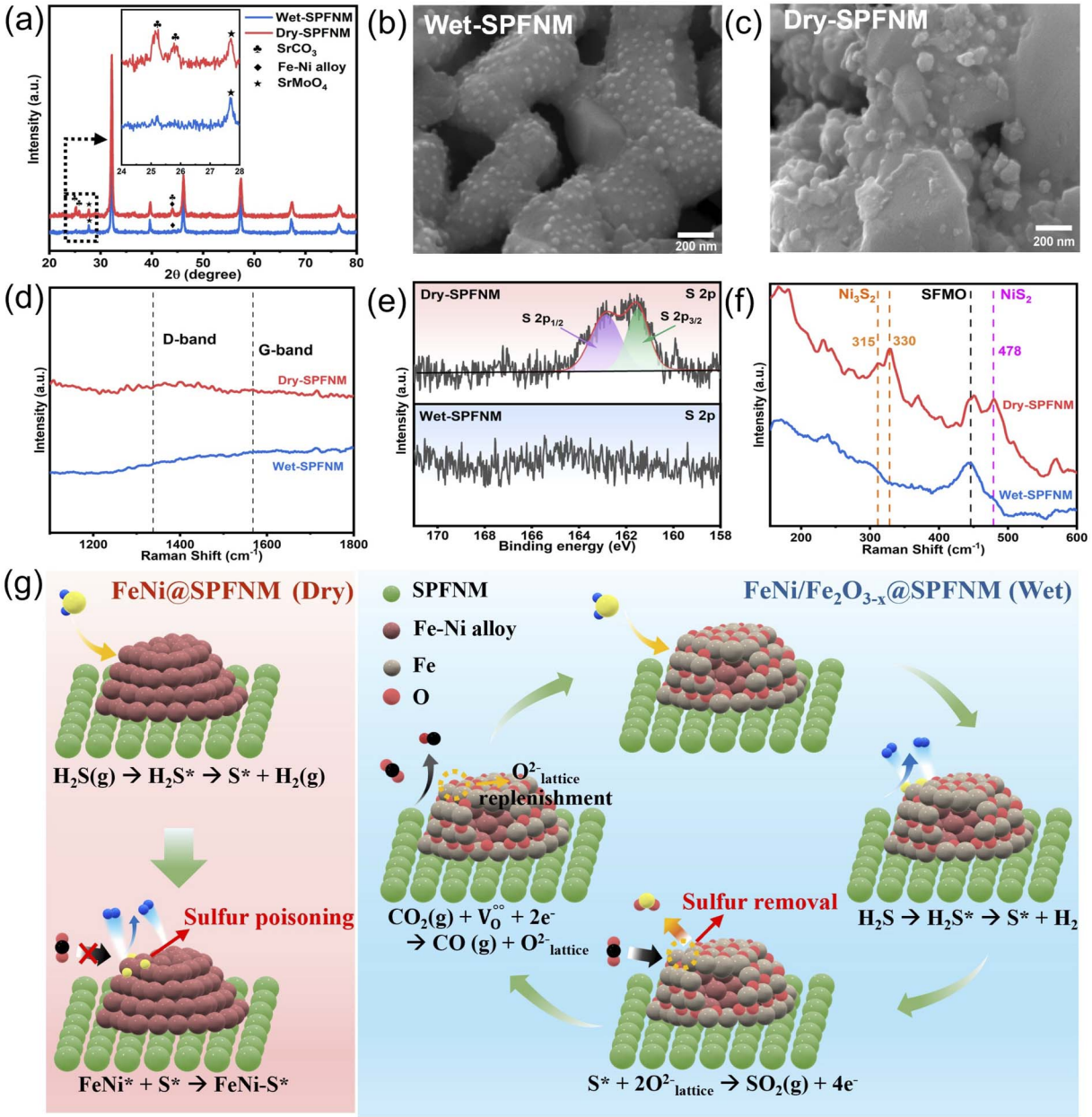

Fig. 6 Characterization of wet-SPFNM and dry-SPFNM after CO_2-separated BFG exposure at 750 °C for 10 hours: (a) XRD patterns, SEM images of (b) wet-SPFNM, (c) dry-SPFNM, (d and f) Raman spectra and (e) S 2p XPS spectra of each sample. (g) Schematic illustration of the proposed sulfur poisoning and tolerance behavior for wet-SPFNM and dry-SPFNM.

which are characteristic of S^{2-} species typically associated with metal sulfides (*e.g.*, Ni_xS_y).[2] In contrast, no discernible S 2p signal was observed for the wet-SPFNM, suggesting negligible surface sulfur accumulation. To further investigate sulfur-related species, Raman spectroscopy was performed. As shown in Fig. 6f, the dry-SPFNM exhibited characteristic peaks at 315 and 330 cm^{-1}, corresponding to Ni_3S_2,[75] and an additional peak at 478 cm^{-1} associated with NiS_2.[76] However, these sulfur-related vibrational features were notably absent in the wet-SPFNM case, indicating that sulfur species formation can be effectively suppressed. To further validate sulfur retention after CO_2-separated BFG exposure, we performed O_2-TPO-MS and monitored the mass signals of $m/z = 64$ (SO_2) and 48 (SO-related fragment). As shown in Fig. S23, dry-SPFNM exhibited clear SO_x evolution peaks centered at around 450 °C in both signals, whereas wet-SPFNM showed no discernible SO_x signal under the identical conditions. Notably, pristine SPFNM also shows no discernible SO_x evolution, indicating intrinsically limited sulfur retention on the oxide surface. This trend is consistent with the general design principle for sulfur-tolerant oxide electrodes based on reversible sulfur redox enabled by lattice oxygen and mobile oxygen ions.[77] Taken together, these results support preferential sulfur retention on dry-SPFNM and strongly suppressed sulfur accumulation on wet-SPFNM, in line

with the XPS and Raman results. To probe the correlation between core–shell thickness and impurity tolerance, an additional 12% wet-SPFNM was examined as a control. While sulfur accumulation remained negligible after CO_2-separated BFG annealing, the reduced exsolution extent and lower vacancy related surface species could result in substantially lower CO_2 electrolysis performance, consistent with the higher pO_2 during reduction that limits further oxygen vacancy formation with the density of CO_2 active sites (Fig. S24). These results suggest that the Fe_2O_{3-x} shell in the exsolved core–shell NPs plays a critical role in mitigating sulfur poisoning. By serving as a physical and chemical barrier, the oxide shell inhibits direct interaction between H_2S and the metallic Fe–Ni alloy core, thereby boosting the sulfur tolerance of the wet-SPFNM under CO_2-separated BFG conditions. In contrast, metallic Fe–Ni alloy NPs exsolved under dry reduction conditions are highly vulnerable to sulfur poisoning, as H_2S readily adsorbs and dissociates on alloy surfaces even at low ppm levels.[12] Upon dissociation, elemental sulfur strongly chemisorbs onto the metal particle surface, leading to the formation of stable nickel sulfide phases (*e.g.*, Ni_xS_y), which severely block active sites and result in irreversible deactivation.[13] This poisoning pathway can be described as follows:

$$H_2S(g) \rightarrow H_2S^* \rightarrow S^* + H_2(g) \quad (2)$$

$$Ni(s) + S^* \rightarrow Ni\text{–}S^* \quad (3)$$

On the other hand, steam-assisted exsolution leads to the formation of $FeNi_3/Fe_2O_{3-x}$ core–shell NPs, where the metallic core is effectively encapsulated by an oxide shell. In this configuration, H_2S is expected to initially interact with the oxide shell, undergoing dissociative adsorption to generate H_2 and elemental sulfur. The adsorbed sulfur species may then be oxidized by lattice oxygen ($B^{(n-1)+}$–V_O–$B^{(n-1)+}$) within the Fe_2O_{3-x} shell, generating gaseous SO_2 which subsequently desorbs from the surface, thereby mitigating sulfur accumulation on the surface.[12,25,78,79] This redox-mediated sulfur oxidation can be described by the following reactions:

$$H_2S(g) \rightarrow H_2S^* \rightarrow S^* + H_2(g) \quad (4)$$

$$S^* + 2O_{lattice}^{2-} \rightarrow SO_2(g) + 4e^- \quad (5)$$

or

$$H_2S(g) + 3O_{lattice}^{2-} \rightarrow SO_2(g) + H_2O(g) + 6e^- \quad (6)$$

Following sulfur oxidation, consumption of lattice oxygen is expected to generate oxygen vacancies ($B^{(n-1)+} - V_O^{\cdot\cdot} - B^{(n-1)+}$) within the Fe_2O_{3-x} shell. In the presence of CO_2 (*e.g.*, BFG), these vacancies could be replenished *via* dissociative activation of CO_2, sustaining the oxidative functionality of the shell. This possible regeneration step can be represented as:

$$CO_2(g) + V_O^{\cdot\cdot} + 2e^- \rightarrow CO(g) + O_{lattice}^{2-} \quad (7)$$

Although direct, real-time observation of such vacancy refilling is beyond the scope of the present study, CO_2-enabled regeneration of redox-active oxides has been largely reported in

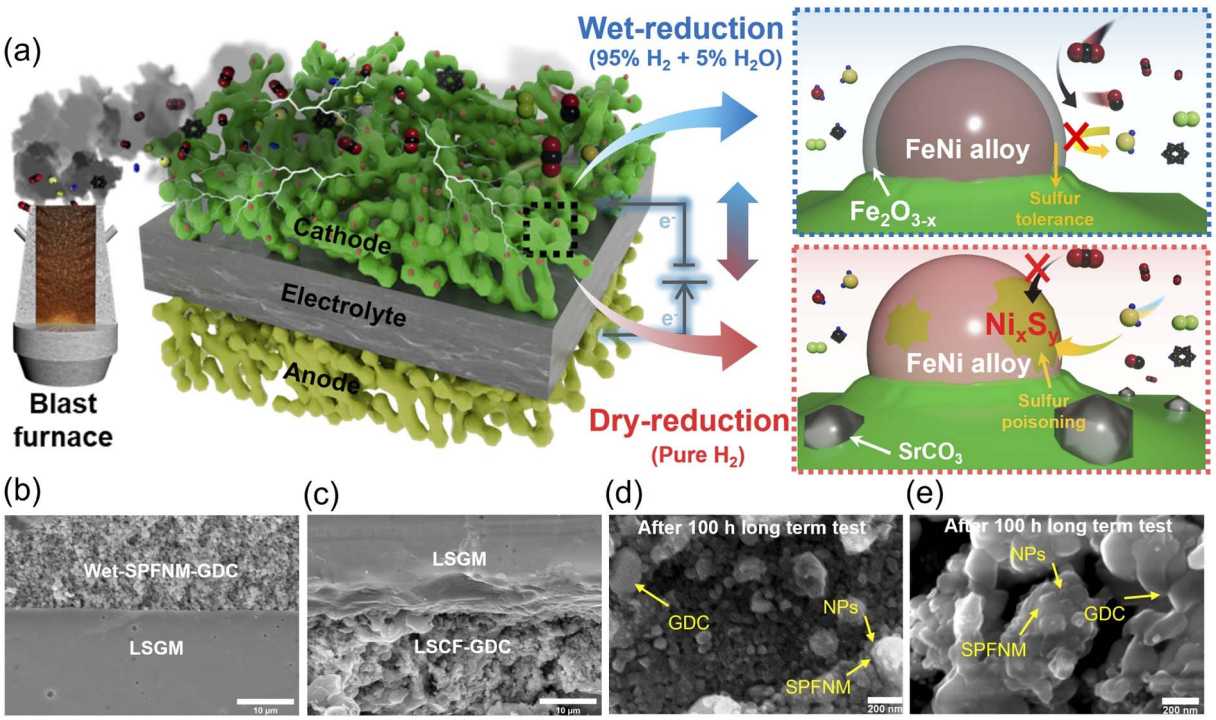

Fig. 7 (a) Schematic illustration of the CO_2 electrolysis process on wet-SPFNM and dry-SPFNM cathodes under BFG conditions. SEM images after 100 h long-term stability test under a constant current of 250 mA cm^{-2} at 750 °C; (b and c) cross-section of a single cell with the wet-SPFNM cathode, (d) wet-SPFNM and (e) dry-SPFNM cathodes.

related systems.[25] Accordingly, we present eqn (7) as a plausible supporting pathway that may contribute to the sustained stability of wet-SPFNM under CO_2-separated BFG operation. Consequently, the improved sulfur tolerance of the wet-SPFNM is reflected in its superior long-term CO_2 electrolysis stability test compared to the dry-SPFNM (Fig. 5g). A schematic illustration of the proposed sulfur tolerance behavior in both samples is presented in Fig. 6g.

Fig. 7a schematically depicts the CO_2 electrolysis process over wet-SPFNM and dry-SPFNM cathodes under a CO_2-separated BFG atmosphere, as inferred from the preceding results. As shown in the cross-sectional SEM images (Fig. 7b and c), the cell with the wet-SPFNM cathode exhibited no evidence of delamination, instead it maintained excellent interfacial adhesion between the electrolyte and electrodes after prolonged operation. Post-mortem SEM analysis after 100 h of electrolysis (Fig. 7d and e) further shows that, in both wet- and dry-SPFNM cathodes, SPFNM and GDC particles remain well-distributed, while the exsolved NPs are firmly anchored to the perovskite matrix.

Conclusion

In summary, we introduced a highly active and sulfur-tolerant SOEC cathode, $Sr_{1.6}Pr_{0.4}Fe_{1.35}Ni_{0.2}Mo_{0.45}O_{6-\delta}$ (wet-SPFNM), functionalized with exsolved $FeNi_3/Fe_2O_{3-x}$ core–shell nanoparticles (NPs) *via* a steam-assisted wet reduction strategy. In single cell tests under simulated blast furnace gas (CO_2-separated BFG), the wet-SPFNM cathode exhibited a 38.9% higher CO_2 electrolysis current density at 750 °C than its conventional dry-reduced counterpart (dry-SPFNM) which features exsolved Fe–Ni NPs. This superior performance is attributed to the unique core–shell nanoarchitecture, which synergistically enriches the surface oxygen vacancies and accelerates the kinetics of CO_2 adsorption and activation. Crucially, the wet-SPFNM cathode single cell exhibited outstanding operational stability, maintaining performance for over 100 h in a CO_2-separated BFG, whereas the dry-SPFNM counterpart underwent rapid degradation. This durability stems from the chemically active Fe_2O_{3-x} shell, which not only serves as a protective barrier preventing direct H_2S exposure on the Fe–Ni alloy core, but also facilitates oxidation of adsorbed sulfur species, thereby mitigating sulfur poisoning. Overall, this study validates the steam-assisted exsolution as a simple yet practical and powerful approach to generate a bifunctional oxide shell, enabling SOEC cathodes with high performance and durability under treated industrial gas streams with trace-level impurities.

Author contributions

S. C. and J. H. contributed equally to this work. S. C. and J. H. conceived the idea. S. C. designed the experiments and wrote the manuscript. S. J. assisted in designing experiments. H. B., J. C., S. K. and Y. Y. assisted in electrochemical measurements. W. B. K. supervised the whole project. All authors discussed the results and commented on the manuscript.

Conflicts of interest

There are no conflicts to declare.

Data availability

The data supporting the findings of this study are available within the article and its supplementary information (SI). Additional datasets generated and analyzed during the current study are available from the corresponding author on reasonable request. Supplementary information: additional catalyst characterization data and electrochemical test data. See DOI: https://doi.org/10.1039/d5ta08830e.

Acknowledgements

This research was supported by Korea Institute of Energy Technology Evaluation and Planning (KETEP) grant funded by the Korea government (MOTIE) (No. 20212010100040), and by the National Research Foundation of Korea (NRF) grant funded by the Korea government (MSIT) (RS-2024-00355916), and by the National Research Foundation of Korea (NRF) grant funded by the Korea government (MSIT) (No. RS-2021-NR060090).

References

1 L. J. Nunes, *Environments*, 2023, **10**, 66, DOI: 10.3390/environments10040066.
2 M. Halmann and A. Steinfeld, *Miner. Process. Extr. Metall. Rev.*, 2015, **36**, 7–12, DOI: 10.1080/08827508.2013.793682.
3 R. T. J. Porter, P. D. Cobden and H. Mahgerefteh, *J. CO_2 Util.*, 2022, **66**, 102278, DOI: 10.1016/j.jcou.2022.102278.
4 J. Kim, H. Lee, B. Lee, J. Kim, H. Oh, I. B. Lee, Y. S. Yoon and H. Lim, *Energy Convers. Manage.*, 2021, **250**, 114922, DOI: 10.1016/j.enconman.2021.114922.
5 M. Riegraf, K. D. Bagarinao, I. Biswas and R. Costa, *J. Power Sources*, 2023, **559**, 232669, DOI: 10.1016/j.jpowsour.2023.232669.
6 Y. Song, X. Zhang, K. Xie, G. Wang and X. Bao, *Adv. Mater.*, 2019, **31**, e1902033, DOI: 10.1002/adma.201902033.
7 J. H. Myung, D. Neagu, D. N. Miller and J. T. Irvine, *Nature*, 2016, **537**, 528–531, DOI: 10.1038/nature19090.
8 Y. Song, Z. Zhou, X. Zhang, Y. Zhou, H. Gong, H. Lv, Q. Liu, G. Wang and X. Bao, *J. Mater. Chem. A*, 2018, **6**, 13661–13667, DOI: 10.1039/C8TA02858C.
9 S. McIntosh and R. J. Gorte, *Chem. Rev.*, 2004, **104**, 4845–4865, DOI: 10.1021/cr020725g.
10 X. L. Shao, R. A. Budiman, T. Sato, M. Yamaguchi, T. Kawada and K. Yashiro, *J. Power Sources*, 2024, **609**, 234651, DOI: 10.1016/j.jpowsour.2024.234651.
11 Y. Wang, W. Li, L. Ma, W. Li and X. Liu, *J. Mater. Sci. Technol.*, 2020, **55**, 35–55, DOI: 10.1016/j.jmst.2019.07.026.
12 Z. Cheng, J. H. Wang, Y. M. Choi, L. Yang, M. C. Lin and M. L. Liu, *Energy Environ. Sci.*, 2011, **4**, 4380–4409, DOI: 10.1039/C1EE01758F.
13 Z. Chu, J. Gao, Q. Lia, T. Xia, L. Sun, H. Zhao, I. V. Kovalev, R. D. Guskov, M. P. Popov and A. P. Nemudry, *J. Mater. Sci.*

Technol., 2025, **212**, 303–311, DOI: 10.1016/j.jmst.2024.06.010.
14 Y. Dou, Y. Xie, X. Hao, T. Xia, Q. Li, J. Wang, L. Huo and H. Zhao, *Appl. Catal., B*, 2021, **297**, 120403, DOI: 10.1016/j.apcatb.2021.120403.
15 J. Choi, D. Jang, M. Kim, J. Ha, H. Ahn and W. B. Kim, *J. Mater. Chem. A*, 2024, **12**, 12619–12627, DOI: 10.1039/D3TA08110A.
16 J. Chen, X. Gao, X. Chen, Z. Zhen, Y. Chen, X. Zeng and L. Cui, *Mater. Today Phys.*, 2023, **38**, 101237, DOI: 10.1016/j.mtphys.2023.101237.
17 H. N. Sun, X. M. Xu, Y. F. Song and Z. P. Shao, *Adv. Funct. Mater.*, 2024, **34**, 2411622, DOI: 10.1002/adfm.202411622.
18 D. Neagu, G. Tsekouras, D. N. Miller, H. Menard and J. T. Irvine, *Nat. Chem.*, 2013, **5**, 916–923, DOI: 10.1038/nchem.1773.
19 S. Park, Y. Kim, H. Han, Y. Chung, W. Yoon, J. Choi and W. B. Kim, *Appl. Catal., B*, 2019, **248**, 147–156, DOI: 10.1016/j.apcatb.2019.02.013.
20 X. Xiong, J. Yu, X. Huang, D. Zou, Y. Song, M. Xu, R. Ran, W. Wang, W. Zhou and Z. Shao, *J. Mater. Sci. Technol.*, 2022, **125**, 51–58, DOI: 10.1016/j.jmst.2022.02.031.
21 H. Lv, T. Liu, X. Zhang, Y. Song, H. Matsumoto, N. Ta, C. Zeng, G. Wang and X. Bao, *Angew. Chem., Int. Ed.*, 2020, **59**, 15968–15973, DOI: 10.1002/anie.202006536.
22 S. V. Mantilla, P. Simon, M. Huvé, G. Gauthier and P. Gauthier-Maradei, *Int. J. Hydrogen Energy*, 2020, **45**, 27145–27159, DOI: 10.1016/j.ijhydene.2020.07.065.
23 J. Li, B. Wei, X. Yue, C. Su and Z. Lü, *Electrochim. Acta*, 2020, **335**, 135703, DOI: 10.1016/j.electacta.2020.135703.
24 D. Liu, Q. Wang, J. Wu and Y. Liu, *Environ. Chem. Lett.*, 2019, **18**, 113–128, DOI: 10.1007/s10311-019-00925-6.
25 J. Hu, H. Poelman, S.-A. Theofanidis, J. J. Joos, C. Detavernier, D. Poelman, W. Wei and V. V. Galvita, *Appl. Catal., B*, 2023, **330**, 122591, DOI: 10.1016/j.apcatb.2023.122591.
26 Y.-H. Lin, Y.-C. Chen and H. Chu, *Chemosphere*, 2015, **121**, 62–67, DOI: 10.1016/j.chemosphere.2014.11.010.
27 Z. Wang, T. Tan, K. Du, Q. Zhang, M. Liu and C. Yang, *Adv. Mater.*, 2024, **36**, 2312119, DOI: 10.1002/adma.202312119.
28 T. Tan, Z. Wang, M. Qin, W. Zhong, J. Hu, C. Yang and M. Liu, *Adv. Funct. Mater.*, 2022, **32**, 2202878, DOI: 10.1002/adfm.202202878.
29 Q. Shao, X. Han, K. Li, W. Guan, Y. Ling and Z. Lv, *J. Colloid Interface Sci.*, 2025, **693**, 137564, DOI: 10.1016/j.jcis.2025.137564.
30 M. Rahm, R. Hoffmann and N. W. Ashcroft, *Chem.–Eur. J.*, 2016, **22**, 14625–14632, DOI: 10.1002/chem.201602949.
31 D. Neagu, V. Kyriakou, I. L. Roiban, M. Aouine, C. Tang, A. Caravaca, K. Kousi, I. Schreur-Piet, I. S. Metcalfe, P. Vernoux and M. C. M. van de Sanden, *ACS Nano*, 2019, **13**, 12996–13005, DOI: 10.1021/acsnano.9b05652.
32 Y. Guo, S. Wang, R. Li, J. C. Yu, X. M. Zhang, M. R. Li, X. S. Zheng, J. Zhu, Y. F. Song, G. X. Wang and X. H. Bao, *Joule*, 2024, **8**, 2016–2032, DOI: 10.1016/j.joule.2024.04.009.
33 X. Y. Chen, W. J. Ni, J. Wang, Q. Zhong, M. F. Han and T. L. Zhu, *Electrochim. Acta*, 2018, **277**, 226–234, DOI: 10.1016/j.electacta.2018.05.019.
34 N. Zhang, W. Zhang, Y. Gong, J. Jun, H. Wang, R. Wang, L. Zhao and B. He, *Adv. Funct. Mater.*, 2025, e15584, DOI: 10.1002/adfm.202515584.
35 H. B. Hu, M. Z. Li, H. H. Min, X. H. Zhou, J. Li, X. Y. Wang, Y. Lu and X. F. Ding, *ACS Catal.*, 2022, **12**, 828–836, DOI: 10.1021/acscatal.1c04807.
36 N. Hou, T. Yao, P. Li, X. Yao, T. Gan, L. Fan, J. Wang, X. Zhi, Y. Zhao and Y. Li, *ACS Appl. Mater. Interfaces*, 2019, **11**, 6995–7005, DOI: 10.1021/acsami.8b19928.
37 S. Shah, J. Hong, L. Cruz, S. Wasantwisut, S. R. Bare and K. L. Gilliard-AbdulAziz, *ACS Catal.*, 2023, **13**, 3990–4002, DOI: 10.1021/acscatal.2c05572.
38 B. W. Zhang, M. N. Zhu, M. R. Gao, X. Xi, N. Duan, Z. Chen, R. F. Feng, H. Zeng and J. L. Luo, *Nat. Commun.*, 2022, **13**, 4618, DOI: 10.1038/s41467-022-32393-y.
39 Z. W. Luo, X. H. Ge, D. Fang, X. F. Xu, D. Zhang, Y. Q. Cao, X. Z. Duan, W. Li, J. H. Zhou and X. G. Zhou, *J. Catal.*, 2024, **434**, 115528, DOI: 10.1016/j.jcat.2024.115528.
40 X. Liu, D. Wang, G. Liu, V. Srinivasan, Z. Liu, Z. Hussain and W. Y ang, *Nat. Commun.*, 2013, **4**, 2568, DOI: 10.1038/ncomms3568.
41 J. Leveneur, G. I. N. Waterhouse, J. Kennedy, J. B. Metson and D. R. G. Mitchell, *J. Phys. Chem. C*, 2011, **115**, 20978–20985, DOI: 10.1021/jp206357c.
42 X. L. Yao, Q. P. Cheng, Y. Attada, S. Ould-Chikh, A. Ramírez, X. Q. Bai, H. O. Mohamed, G. X. Li, G. Shterk, L. R. Zheng, J. Gascon, Y. Han and O. M. Bakr, *Appl. Catal., B*, 2023, **328**, 122479, DOI: 10.1016/j.apcatb.2023.122479.
43 J. Jiang, M. Wang, W. S. Yan, X. F. Liu, J. X. Liu, J. L. Yang and L. C. Sun, *Nano Energy*, 2017, **38**, 175–184, DOI: 10.1016/j.nanoen.2017.05.045.
44 H. Hou, M. Han, B. Wang, Y. Cong, K. Huang, X. Hou, Y. Zhang, B. Zheng and S. Feng, *Adv. Energy Mater.*, 2025, **15**, 2402925, DOI: 10.1002/aenm.202402925.
45 D. N. Wang, J. G. Zhou, Y. F. Hu, J. L. Yang, N. Han, Y. G. Li and T. K. Sham, *J. Phys. Chem. C*, 2015, **119**, 19573–19583, DOI: 10.1021/acs.jpcc.5b02685.
46 S. Zhai, R. B. Zhao, H. L. Liao, L. Fu, S. R. Hao, J. Y. Cai, Y. F. Wu, J. Wang, Y. H. Jiang, J. Xiao, T. Liu and H. P. Xie, *J. Energy Chem.*, 2024, **96**, 39–48, DOI: 10.1016/j.jechem.2024.04.011.
47 H. Lv, L. Lin, X. Zhang, D. Gao, Y. Song, Y. Zhou, Q. Liu, G. Wang and X. Bao, *J. Mater. Chem. A*, 2019, **7**, 11967–11975, DOI: 10.1039/C9TA03065D.
48 I. Waluyo and A. Hunt, *Synchrotron Radiat. News*, 2022, **35**, 31–38, DOI: 10.1080/08940886.2022.2082180.
49 C. Yuan, D. Feng, H. Ye, P. Shan, L. Ge, H. Chen, Y. Zheng and S. Cui, *J. Mater. Chem. A*, 2025, **13**, 32562–32576, DOI: 10.1039/D5TA05724H.
50 F. Fang, N. J. Feng, P. Zhao, C. Chen, X. Li, J. Meng, G. Liu, L. Chen, H. Wan and G. F. Guan, *Chem. Eng. J.*, 2019, **372**, 752–764, DOI: 10.1016/j.cej.2019.04.176.

51 S. Q. Hu, L. X. Zhang, H. Y. Liu, Z. W. Cao, W. G. Yu, X. F. Zhu and W. S. Yang, *J. Power Sources*, 2019, **443**, 227268, DOI: 10.1016/j.jpowsour.2019.227268.
52 W. Wang, H. Li, C. Y. R. Vera, J. Lin, K.-Y. Park, T. Lee, D. Ding and F. Chen, *J. Mater. Chem. A*, 2023, **11**, 9039–9048, DOI: 10.1039/D3TA00186E.
53 F.-Z. Han, Z.-X. Wang, S.-L. Zhang, C.-X. Li and S. A. Barnett, *Appl. Catal., B*, 2025, **361**, 124676, DOI: 10.1016/j.apcatb.2024.124676.
54 S. Zhang, Y. Jiang, H. Han, Y. Li and C. Xia, *ACS Appl. Mater. Interfaces*, 2022, **14**, 28854–28864, DOI: 10.1021/acsami.2c05324.
55 M. Wang, Y. Da, M. Xie and Z. Wang, *J. Power Sources*, 2025, **634**, 236498, DOI: 10.1016/j.jpowsour.2025.236498.
56 Y. Luo, D. Zhang, T. Liu, X. Chang, J. Wang, Y. Wang, X. K. Gu and M. Ding, *Adv. Funct. Mater.*, 2024, **34**, 2403922, DOI: 10.1002/adfm.202403922.
57 Z. Liu, J. Zhou, Y. Sun, X. Yue, J. Yang, L. Fu, Q. Deng, H. Zhao, C. Yin and K. Wu, *J. Energy Chem.*, 2023, **84**, 219–227, DOI: 10.1016/j.jechem.2023.05.033.
58 Y. Li, Y. Li, S. Zhang, C. Ren, Y. Jing, F. Cheng, Q. Wu, P. Lund and L. Fan, *ACS Appl. Mater. Interfaces*, 2022, **14**, 9138–9150, DOI: 10.1021/acsami.1c23548.
59 S. W. Lee, T. H. Nam, M. Kim, S. Lee, K. H. Lee, J. H. Park and T. H. Shin, *Inorg. Chem. Front.*, 2023, **10**, 3536–3543, DOI: 10.1039/D3QI00379E.
60 S. Lee, M. Kim, K. T. Lee, J. T. Irvine and T. H. Shin, *Adv. Energy Mater.*, 2021, **11**, 2100339, DOI: 10.1002/aenm.202100339.
61 S. W. Lee, T. H. Nam, T. Ishihara, J. T. Irvine and T. H. Shin, *Energy Environ. Sci.*, 2025, **18**, 1205–1213, DOI: 10.1039/D4EE03893B.
62 X. Wang, H. Hu, C. Xie, Y. Wang, H. Li and X. Ding, *J. Mater. Chem. A*, 2024, **12**, 11701–11709, DOI: 10.1039/D3TA07820E.
63 M. Emadi and E. Croiset, *J. Mater. Chem. A*, 2026, **14**, 5682–5694, DOI: 10.1039/D5TA07206A.
64 Y. Zhu, N. Zhang, W. Zhang, Y. Gong, R. Wang, H. Wang, J. Jin, L. Zhao and B. He, *J. Mater. Chem. A*, 2024, **12**, 18182–18192, DOI: 10.1039/D4TA02372B.
65 F. Hu, Y. Ling, S. Fang, L. Sui, H. Xiao, Y. Huang, B. He and L. Zhao, *Appl. Catal., B*, 2023, **337**, 122968, DOI: 10.1016/j.apcatb.2023.122968.
66 L.-B. Liu, S. Liu, M. Yang, Y. Li, B. Ouyang, P. Zhang, X.-Z. Fu, Y. Sun, S. Liu and J.-L. Luo, *Appl. Catal., B*, 2025, **379**, 125705, DOI: 10.1016/j.apcatb.2025.125705.
67 Y. Shen, S. Wang, X. Chen, H. Lv, Y. Guo, H. Liu, H. Zhao, N. Ta, M. Li, X. Zhang, Y. Song, G. Wang and X. Bao, *J. Am. Chem. Soc.*, 2025, **147**(35), 31821–31828, DOI: 10.1021/jacs.5c09067.
68 D. Liu, H. Shang, C. Zhou, J. Miao, D. Xu, Z. Chen, M. Fei, F. Liang, Q. Niu, R. Ran, W. Zhou and Z. Shao, *Energy Environ. Mater.*, 2024, **7**(5), e12717, DOI: 10.1002/eem2.12717.
69 X. Xi, Y. Fan, J. Zhang, J.-L. Luo and X.-Z. Fu, *J. Mater. Chem. A*, 2022, **10**, 2509–2518, DOI: 10.1039/D1TA07678G.
70 Y.-H. Huang, G. Liang, M. Croft, M. Lehtimaki, M. Karppinen and J. B. Goodenough, *Chem. Mater.*, 2009, **21**, 2319–2326, DOI: 10.1021/cm8033643.
71 T. F. Winterstein, C. Malleier, B. Klötzer, V. Kahlenberg, C. Hejny, M. F. Bekheet, J. T. Müller, A. Gurlo, M. Heggen and S. Penner, *Mater. Today Chem.*, 2024, **41**, 102255, DOI: 10.1016/j.mtchem.2024.102255.
72 L. dos Santos-Gómez, L. León-Reina, J. M. Porras-Vázquez, E. R. Losilla and D. Marrero-López, *Solid State Ionics*, 2013, **239**, 1–7, DOI: 10.1016/j.ssi.2013.03.005.
73 F. Orsini, D. Ferrero, S. F. Cannone, M. Santarelli, A. Felli, M. Boaro, C. de Leitenburg, A. Trovarelli, J. Llorca, G. Dimitrakopoulos and A. F. Ghoniem, *Chem. Eng. J.*, 2023, **475**, 146083, DOI: 10.1016/j.cej.2023.146083.
74 A. López-García, L. Almar, S. Escolástico, A. B. Hungría, A. J. Carrillo and J. M. Serra, *ACS Appl. Energy Mater.*, 2022, **5**, 13269–13283, DOI: 10.1021/acsaem.2c01829.
75 Z. Cheng, H. Abernathy and M. L. Liu, *J. Phys. Chem. C*, 2007, **111**, 17997–18000, DOI: 10.1021/jp0770209.
76 S.-L. Yang, H.-B. Yao, M.-R. Gao and S.-H. Yu, *CrystEngComm*, 2009, **11**, 1383–1390, DOI: 10.1039/B900444K.
77 P. Boldrin, E. Ruiz-Trejo, J. Mermelstein, J. M. Bermúdez Menéndez, T. R. Reina and N. P. Brandon, *Chem. Rev.*, 2016, **116**, 13633–13684, DOI: 10.1021/acs.chemrev.6b00284.
78 Z. Cheng, S. W. Zha and M. L. Liu, *J. Power Sources*, 2007, **172**, 688–693, DOI: 10.1016/j.jpowsour.2007.07.052.
79 J. N. Gu, J. X. Liang, L. J. Wang, Y. X. Xue, K. Li, M. M. Guo, T. H. Sun and J. P. Jia, *J. Hazard. Mater.*, 2025, **494**, 138714, DOI: 10.1016/j.jhazmat.2025.138714.

